

# Chapter 2

## Data Analysis

### 2.1 Introduction

As discussed in chapter-I, x-ray diffraction and freeze fracture electron microscopy are the two techniques commonly used to probe the equilibrium structure of the ripple ( $P_{\beta'}$ ) phase of phospholipids. We have used the x-ray diffraction method to determine electron density maps of the ripple phase for different lipids and lipid mixtures. An electron density map (EDM) gives the local density of electrons (and hence atoms) that scatter x-rays within a unit cell [1]. We have analyzed data mainly from four sources: (1) data from unoriented sample of DMPC obtained using a synchrotron source, reported by Wack and Webb in ref. [2], (2) data from oriented samples of DMPC and POPC taken by Raghunathan and Katsaras [3] using a rotating anode x-ray generator, (3) data from oriented samples of DHPC and mixtures of DPPC and DHPC taken in our own laboratory again using a rotating anode generator and (4) data from unoriented samples of DLPC reported by Tardieu et. al. in ref. [4]. Other data available in the literature have too many overlapping reflections to be suitable for this kind of analysis [5]. In this chapter, we first give an introduction to x-ray diffraction. In section-2.2 we discuss the details of the experimental procedure and in section-2.3 the procedure for data reduction, with special reference to the problem of applying absorption correction to data from samples aligned in the geometry specific to our experiment. The modeling and fitting procedure used to calculate the phases of the reflections is described in sections-2.4 and -2.5. The electron density maps

obtained by this procedure will be discussed in chapter-III.

### 2.1.1 Diffraction and Fourier transform

The scattering of x-rays by a single electron can be described by Thompson scattering where the electron is free and the wavelengths of the incident and the scattered radiations are the same. If the electric field associated with the incident radiation is  $E_{in}$ , then the electric field associated with the scattered wave can be written as  $E_{scat} = f_e E_{in}$ ;  $f_e$  is called the electronic scattering factor and represents the ability of the electron to scatter radiation. It depends on fundamental constants and is an intrinsic property of electrons.

The scattering from an array of  $n$  electrons results in vector addition of the electric fields associated with the radiation scattered from each electron  $E_{scat} = \sum_n f_e e^{i\Phi_n} E_{in}$ , where  $\Phi$  is a phase factor that is determined by the relative positions of the electrons and the wavelength of the incident wave. For the  $j^{th}$  electron,  $\Phi_j = \mathbf{q} \cdot \mathbf{r}_j$ , where  $\mathbf{q}$  is the reciprocal lattice vector and  $\mathbf{r}_j$  the position vector of the electron. In case of a continuous distribution of electrons, the scattering by a volume element is given by  $dE_{scat} = f_e \rho(\mathbf{r}) d\mathbf{r}$  where  $\rho(\mathbf{r})$  is the density of electrons,  $\rho(\mathbf{r}) d\mathbf{r}$  is the number of electrons in the volume element  $d\mathbf{r}$ . Therefore the total scattered amplitude is given by

$$F(\mathbf{q}) = \int_{all \mathbf{r}} f_e \rho(\mathbf{r}) e^{i\mathbf{q} \cdot \mathbf{r}} d\mathbf{r}$$

Thus it is clear that the scattered amplitude from an object whose structure is described by a function  $\rho(\mathbf{r})$ , is the Fourier transform  $F(\mathbf{q})$  of  $\rho(\mathbf{r})$ . In case of x-rays, the electrons are the scattering centers and therefore  $\rho(\mathbf{r})$  describes the distribution of electrons in space. The structure of a periodic object (a crystal or a liquid crystal for example) can be described by a convolution of the structure of the lattice  $[\rho(\mathbf{r})]_{lattice}$  with the structure of the basis  $[\rho(\mathbf{r})]_{basis}$ :

$$\rho(\mathbf{r}) = [\rho(\mathbf{r})]_{lattice} * [\rho(\mathbf{r})]_{basis}$$

Therefore, in Fourier space, the Fourier transforms are related by:

$$F(\mathbf{q}) = [F(\mathbf{q})]_{lattice} \cdot [F(\mathbf{q})]_{basis}$$

In real space,

$$[\rho(\mathbf{r})]_{lattice} = \sum_{n_1, n_2, n_3} \delta(\mathbf{r} - [n_1 \mathbf{a} + n_2 \mathbf{b} + n_3 \mathbf{c}])$$

where  $\mathbf{a}$ ,  $\mathbf{b}$  and  $\mathbf{c}$  are the basis vectors and  $n_1$ ,  $n_2$  and  $n_3$  are integers. Therefore

$$[F(\mathbf{q})]_{lattice} = \sum_{h, k, l} \delta(\mathbf{q} - (h\mathbf{a}^* + k\mathbf{b}^* + l\mathbf{c}^*))$$

where  $\mathbf{a}^*$ ,  $\mathbf{b}^*$  and  $\mathbf{c}^*$  are the basis vectors in the reciprocal space and  $h, k, l$  are integers.

The form factor  $[F(\mathbf{q})]_{basis}$  is determined by the scattering from the contents of one unit cell. The amplitude of the diffraction pattern from the crystal, called the structure factor, is the form factor of the unit cell sampled at the reciprocal lattice points  $\mathbf{q}_{hkl} = h\mathbf{a}^* + k\mathbf{b}^* + l\mathbf{c}^*$ . It is given by

$$F_{hkl} = \int_{unit\ cell} \rho(\mathbf{r}) e^{i\mathbf{q}_{hkl} \cdot \mathbf{r}} d\mathbf{r} \quad (2.1)$$

### 2.1.2 The phase problem

In an x-ray experiment, only the intensities ( $|F_{\mathbf{q}}|^2$ ), and not the structure factors ( $F_{\mathbf{q}}$ ) themselves are recorded. But  $|F_{\mathbf{q}}|^2 = |F_{\mathbf{q}} e^{i\Phi}|^2$  where  $\Phi$  can be any real number. For a centrosymmetric object,  $\rho(\mathbf{r}) = \rho(-\mathbf{r})$ . Thus, when the Fourier integral is calculated, the imaginary part of the integrand is an odd function and integrates to zero whereas the real part is an even function and contributes to the Fourier transform. Therefore the Fourier transform of a centrosymmetric function is real and scattering from a centrosymmetric object gives rise to  $e^{i\Phi} = \pm 1$ .

The information about the phase  $\Phi$  is lost when only intensities are recorded. The major challenge in determination of crystal structure from x-ray data involves the determination of the phases of the reflections. Once the phases are known, the electron density can be reconstructed by inverting eq.-2.1; that is, by taking the inverse Fourier transform of  $F(\mathbf{q})$ :

$$\begin{aligned}
\rho(\mathbf{r}) &= \sum_{\mathbf{q}} F(\mathbf{q}) e^{-i\mathbf{q}\cdot\mathbf{r}} \\
&= \sum_{h,k,l} F_{hkl} e^{-i\mathbf{q}_{hkl}\cdot\mathbf{r}}
\end{aligned} \tag{2.2}$$

## 2.2 Experimental procedure

### 2.2.1 Temperature and humidity control:

A locally built temperature and humidity controlled heater was used to collect data from oriented samples of DHPC, DPPC and their mixtures. The heater consists of an air tight nickel-plated brass chamber with a double wall through which water can be circulated. Temperature of the heater is controlled (to within  $\pm 0.5^\circ\text{C}$ ) by circulating suitably heated (or cooled) water. The chamber has an entrance and an exit window for the x-rays. These windows are covered by mylar sheets. A humidity and temperature sensor (*Testo 610*) is introduced into the chamber to monitor these parameters. A small electric fan is placed inside to induce air flow and thus keep the humidity and temperature inside as uniform as possible. The humidity is maintained by placing a saturated salt solution inside the chamber. The salt solution equilibrates with the atmosphere inside the chamber and thus the humidity is maintained (to within  $\pm 2\%$ ) at a value fixed by the specific salt solution used. A schematic diagram of the heater is given in figure 2.1.

While working at temperatures more than a few degrees above the room temperature, moisture condensation on the inner surface of the windows which are at a slightly lower temperature has to be prevented by heating them from outside. This moisture condensation disturbs the humidity balance inside the chamber. The heating is done by blowing warm air onto the mylar windows from outside.

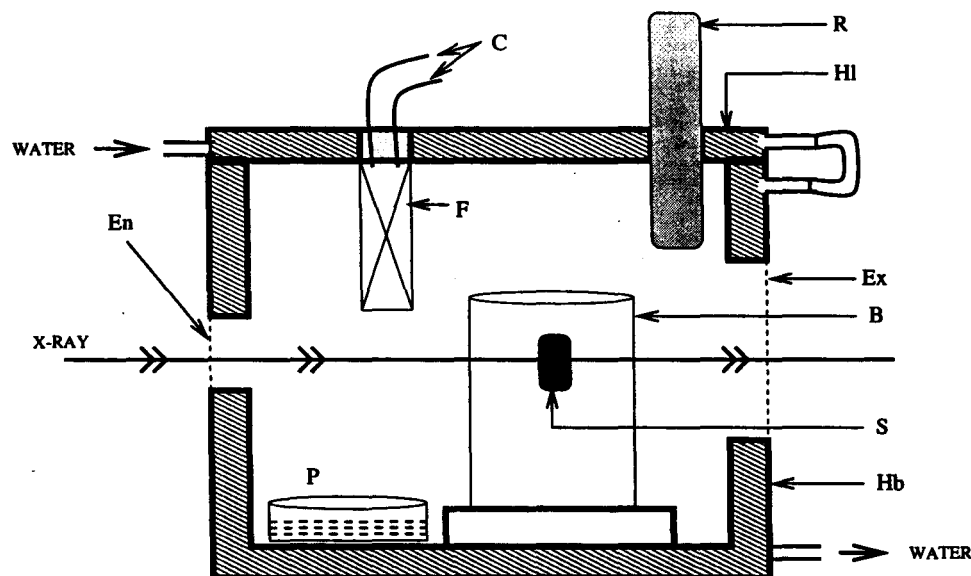


Figure 2.1: A schematic diagram of the humidity controlled heater used to collect data from aligned samples. Hl and Hb : the lid and the body of the heater, the double walls through which temperature controlled water is circulated is indicated by shading. En and Ex: the entrance and exit windows for the x-ray - both covered with mylar sheets. R: the temperature and humidity sensor. B: beaker on which the sample is deposited. S: deposited sample. P: petri-dish with salt solution to control the humidity inside. F: fan to circulate air. C: electrical connections for the fan.

## 2.2.2 Sample preparation

All the lipids studied were obtained from *Sigma chemical Co.* and were used as received. The sample is prepared by dissolving desired amounts of the lipid in a solvent (methyl alcohol in our case) and then spraying a little of the solution on the convex surface of a glass beaker (radius  $\approx 1.5$  cm). The solvent is then evaporated off by placing the beaker in an evacuated dessicator for about one hour. To hydrate the sample, it is sealed in an air tight container along with some pure water for about two days. A relative humidity (RH) of about  $98 \pm 2\%$  can be achieved in our heater by this method. A suitable salt solution is used instead of pure water if a humidity less than  $\approx 98\%$  is required. The sample is cycled up and down through the main and pre transitions a few times to facilitate hydration and alignment. A stack of bilayers, all oriented parallel to the curved glass surface is obtained by this method.

An unoriented sample consists of many randomly oriented domains within each of

which there is a high degree of positional and orientational correlation. The present method of preparing the sample orients the bilayers parallel to the substrate, but the ripple direction does not get fixed. This means that the domains are oriented at random with respect to the ripple direction but are all correlated with respect to the layering direction. Therefore the sample is oriented along the layer normal but is unoriented in the plane perpendicular to the layer normal.

Now, in order to sample more than one Bragg spot, normally an oriented sample has to be rotated while being exposed to x-rays. By depositing the sample on a curved surface, we get rid of the problem of rotating the sample. In this case, the curvature of the orienting surface introduces artificially the mosaicity that is necessary in order to scan many reflections simultaneously. But this means that different parts of the sample diffract into different Bragg-spots (see figure-2.2) and hence the absorption-correction (discussed in section-2.3.3) for each reflection is different.

### 2.2.3 Data collection

Cu  $K_\alpha$  ( $\lambda = 1.54 \text{ \AA}$ ) radiation from a rotating anode x-ray generator (*Rigaku, UltraX 18*) operating at 50kV and 80mA is used to illuminate the sample. A flat graphite monochromator (*Huber*) is used to make the incident x-rays monochromatic. The data is collected by an image plate (*Marresearch*, diameter 180 mm) which is connected to a computer with its own built-in software for data collection. Typical sample to film distance is about 200 mm and typical exposures last for about five hours. The images are obtained as gray scale plots of the intensity and are in the form of binary files. They have to be first converted to a form readable by standard softwares. We use the general purpose mathematical software package 'matlab' to read the intensities. The image is displayed using 'matlab' and the spot to be integrated is identified. A box is drawn around the spot and the contents of this box is redisplayed separately. The local contribution from the background is calculated by finding the average intensity of the pixels just outside the extent of the spot. The box

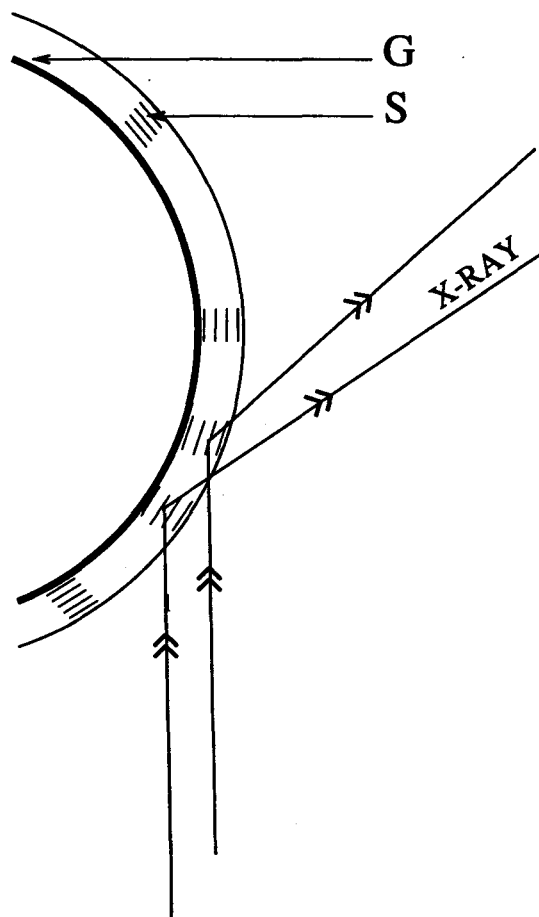


Figure 2.2: **The geometry of the sample.** G: glass surface of the beaker; S: deposited sample. The bilayers (indicated by set of parallel lines) are oriented parallel to the glass surface. In different parts of the sample, the bilayers make different angles with respect to the incident beam and hence different parts of the sample diffract into different Bragg angles.

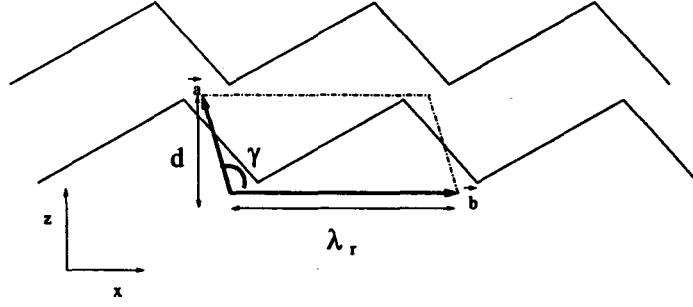


Figure 2.3: Real space unit cell for asymmetric ripples.

should be large enough to contain all the high intensity pixels corresponding to the spot in question but not so large that it includes contributions from the neighboring spots. The average background intensity is subtracted from each pixel in the box and then the intensities of all the pixels inside the box are added up to get the total integrated intensity. The precise extent of the box is not important as long as the background subtraction is done properly. For the DHPC diffraction patterns, the binary files were directly displayed and manipulated by a locally written program that uses the image handling routines 'pg-plot' to display the image.

## 2.3 Data reduction

### 2.3.1 The unit cell

In the  $P_{\beta'}$  phase, the ripples in the different bilayers are in registry and thus form a two dimensional oblique lattice (figure-2.3). The unit cell vectors are given by:

$$\mathbf{a} = d \cot \gamma \hat{x} + d \hat{z}$$

$$\mathbf{b} = \lambda_r \hat{x}$$

where  $\lambda_r$  is the ripple wavelength,  $d$  is the lamellar spacing and  $\gamma$  is the oblique angle.

The lattice vectors in the reciprocal space are therefore given by:

$$\mathbf{A} = \frac{2\pi}{d} \hat{q}_z$$

$$\mathbf{B} = \frac{2\pi}{\lambda_r} \hat{q}_x - \frac{2\pi}{\lambda_r \tan \gamma} \hat{q}_z$$



where  $\hat{q}_x$  and  $\hat{q}_z$  are vectors in the reciprocal space corresponding to the real space vectors  $\hat{x}$  and  $\hat{z}$ . The angle between the basis vectors in the reciprocal lattice is  $\pi - \gamma$ .

Therefore the q-space vector  $\mathbf{q}_{hk}$  for the Bragg peak with Miller indices  $(h, k)$  is:

$$\begin{aligned}\mathbf{q}_{hk} &= h\mathbf{A} + k\mathbf{B} \\ &= \frac{2\pi k}{\lambda_r} \hat{q}_x + \left( \frac{2\pi h}{d} - \frac{2\pi k}{\lambda_r \tan \gamma} \right) \hat{q}_z\end{aligned}\quad (2.3)$$

In the above discussion, the rippling direction is the  $\hat{x}$  direction and the bilayer stacking is along  $\hat{z}$  direction. In that case, the spots along  $q_z$  (ie. the  $(h, 0)$  reflections) correspond to the layer spacing and are called the main reflections. The other spots (with  $k \neq 0$ ) arise due to the ripples and form an "X"-pattern around the main reflections, as the rippling direction is not oriented. These are called satellite reflections or simply satellites (a typical diffraction pattern is given in figure-2.4). The ripple-wavelength ( $\lambda_r$ ), the bilayer repeat distance ( $d$ ) and the oblique angle ( $\gamma$ ) can thus be directly read off from the diffraction pattern. To get the other more subtle characteristics of the ripple profile; for example the actual shape, the sawtooth amplitude and the bilayer thickness etc., the electron density map has to be calculated.

### 2.3.2 Geometric corrections

In a real system, because of various effects like finite extension of the sample, the finite angular spread of the incident beam coupled to the mosaicity of the sample, etc., the reciprocal lattice points are not mathematical points but are smeared out patches. In an experiment, the intersection of this smeared-out reciprocal lattice point with the Ewald sphere is recorded. To facilitate this intersection, the sample is usually either rotated or is taken in the form of randomly oriented crystallites so that the Bragg spots become arcs or rings. In the present case the sample is deposited on a curved surface and this increases the effective mosaicity of the sample in the direction of curvature and the Bragg spots become arcs that subtends an angle  $\Delta$  at the origin of the reciprocal space. Since  $\Delta$  is the same for all the spots, the smearing-out is more

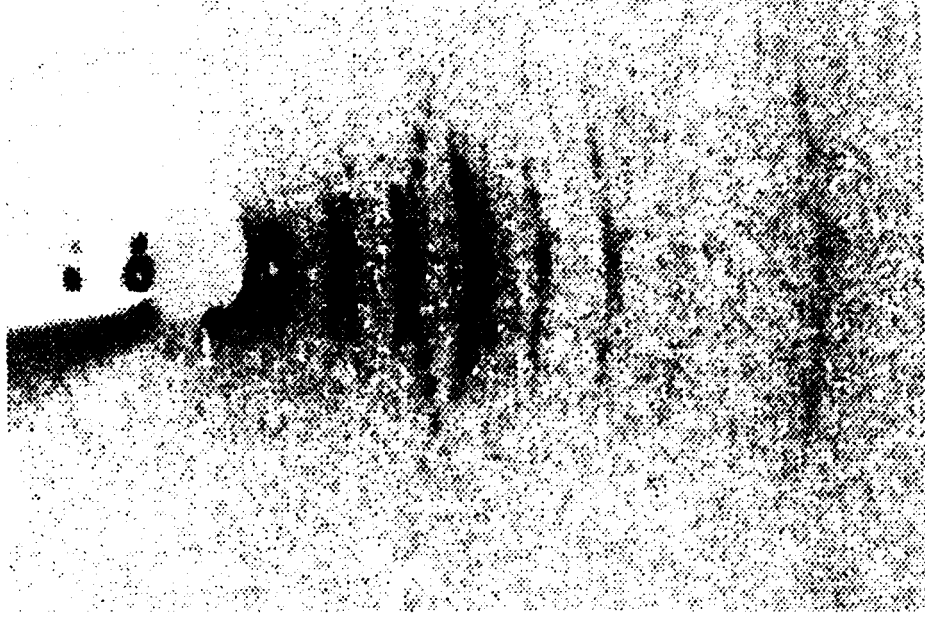


Figure 2.4: A typical diffraction pattern from the ripple phase (DMPC).

for larger scattering angles (see figure-2.5). This leads to a large reduction in the observed intensity of the reflections. To correct for this effect, the observed intensity has to be multiplied by the length of the arc which is given by  $\frac{4\pi}{\lambda} \sin\theta \Delta$ , where  $\lambda$  is the wavelength of the incident x-rays and  $\theta$  the corresponding Bragg angle. This arc has a finite width and what is recorded is the cross-section of this with the Ewald sphere. As the Ewald sphere cuts the arc at an angle  $\theta$ , a further factor of  $\cos\theta$  is present. The corrected intensity is given by:

$$I_{real} = I_{ob} \frac{4\pi}{\lambda} \sin\theta \cos\theta \Delta \quad (2.4)$$

$I_{real}$  is the corrected intensity,  $I_{ob}$  is the observed intensity and  $\Delta$  is the estimated mosaicity; see figure-2.5 for an explanation of how  $\Delta$  is estimated.

While applying geometrical corrections to the observed intensities we have to take into account the fact that the sample is unoriented in two dimensions and oriented in the third direction; that is, lamellae are oriented parallel to the glass surface but the ripple direction is not fixed. We assume that the ripple orientation is uniformly distributed, that is, all orientations are equally possible. For the lamellar reflections, the previous discussion holds and the corrected intensities can be calculated using eq.-2.4.

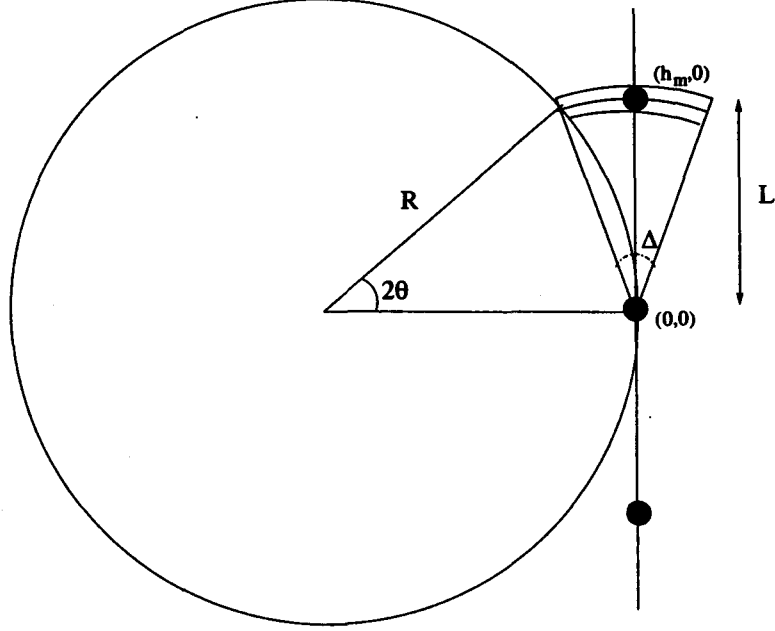


Figure 2.5: Geometrical correction for the main reflections.  $(h_m, 0)$  is the highest order reflection detected. The circle of radius  $R = \frac{2\pi}{\lambda}$  represents the Ewald sphere. The angular spread of the  $(h, 0)$  reflections is  $\Delta$ . This corresponds to a linear spread of  $L\Delta$  where  $L$  is the distance (in reciprocal space) between the  $m^{\text{th}}$  order and the origin;  $L = 4\pi \sin(\theta)/\lambda$ . From simple geometric constructions, the condition for the  $m^{\text{th}}$  order reflection, corresponding to a Bragg angle  $\theta_m$ , to intersect the Ewald sphere is:  $\Delta = 2\theta_m$ . To estimate  $L$ , it is assumed that the angular spread in the  $L_{\beta'}$  phase and the  $P_{\beta'}$  phase are the same. The highest order reflection visible in the  $L_{\beta'}$  phase is the 8th order. This gives a lower limit for  $L$  since it is possible that the higher order reflections are present but are too faint to be detected. Another way of estimating  $L$  is from the fact that for the highest order recorded, the angle  $\Delta$  is given by  $\cos\Delta = (r - w)/r$  where  $r$  is the radius of the beaker and  $w$  is the beam width ( $\approx 1$  mm). The two estimates are comparable and typically,  $\Delta \approx 10^\circ$ .

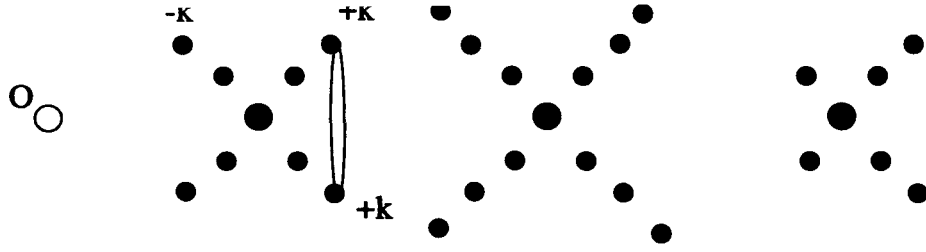


Figure 2.6: Schematic diagram of a typical diffraction pattern from the ripple phase. The open circle marked 'O' corresponds to the origin. The big filled circles are the main reflections and the small filled circles are the satellite reflections. The  $+k$  and  $-k$  reflections are marked. Each satellite is a ring which cuts the Ewald sphere twice thus giving rise to two spots.

Since the direction of the ripple is not fixed, the satellite reflections form a ring around each lamellar reflection (fig. 2.6). The observed spots are where these rings intersect the Ewald sphere, each ring thus gives rise to two equivalent spots. Because of the smearing effect discussed before, the cross-section of the ring broadens. This ring intersects the Ewald sphere at a small angle and so the total integrated intensity of the spot has a very weak angular dependence (proportional to cosine of the angle), provided it is cut twice and not once only at its edge. Thus the correction due to the mosaic spread is automatically taken care of. But this is only a cross-section and so has to be multiplied by the perimeter of the ring to get the total intensity. The radius of this ring is  $\frac{2\pi|k|}{\lambda_r} \sin\gamma$  where  $k$  is the corresponding Miller index. Therefore for the satellites,

$$I_{real} = I_{ob} \frac{4\pi^2}{\lambda_r} |k| \sin\gamma \quad (2.5)$$

where,  $I_{real}$  is the corrected intensity and  $I_{ob}$  is the observed intensity. The numerical factors have to be taken care of properly since unlike in a fully oriented or fully unoriented sample, the numerical factors for lamellar and satellite reflections are different.

### 2.3.3 Absorption corrections

As the x-rays travel through the sample, they get absorbed and thus lose some of their intensity. This happens both before and after scattering. In the present geom-

etry, unlike in conventional powder samples, different parts of the samples diffract into different orders (figure-2.2). Therefore the path traveled inside the medium, and hence the absorption correction, is different for each order. For this reason, absorption corrections may be quite important here.

To calculate the absorption, it is assumed that the glass surface on which the sample is deposited, is opaque to x-rays. The path traveled (before and after scattering) by x-rays diffracted from each part of the sample is calculated from geometrical considerations. The absorption coefficient ( $\mu$ ) is estimated (from the values of the atomic absorption coefficients given in standard tables and using the volumetric data of Wiener et. al. [6]), to be equal to 9/unit length. The absorption corrected intensity is given by:

$$I_{abcorr} = I / \int_{l=0}^{\delta} e^{-\mu p(l)} dl \quad (2.6)$$

where  $p(l)$  is the path traveled by the x-rays inside the medium (see figure-2.7 for the expression for  $p(l)$ ). Here  $\delta$  is the thickness of the sample,  $R$  is the radius of the beaker on which the sample is deposited,  $\theta$  is the Bragg angle for that reflection.

Since the thickness of the sample is difficult to measure, we have not been able to take absorption corrections into account. To check if this omission seriously affects our final electron density maps, we have assumed some reasonable values for the thickness (of the order of 10 - 100 microns) and applied the corrections. We find that the final electron density map is not affected much by these corrections. Therefore we are justified in neglecting absorption in the calculations presented here for the oriented samples.

## 2.4 Modeling of the ripples

As discussed before, only the intensities ( $|F_q|^2$ ) and not the structure factors ( $F_q$ ) themselves are recorded in a x-ray diffraction experiment. The major task is therefore to find the phase of each reflection. We have adopted a modeling and least squares

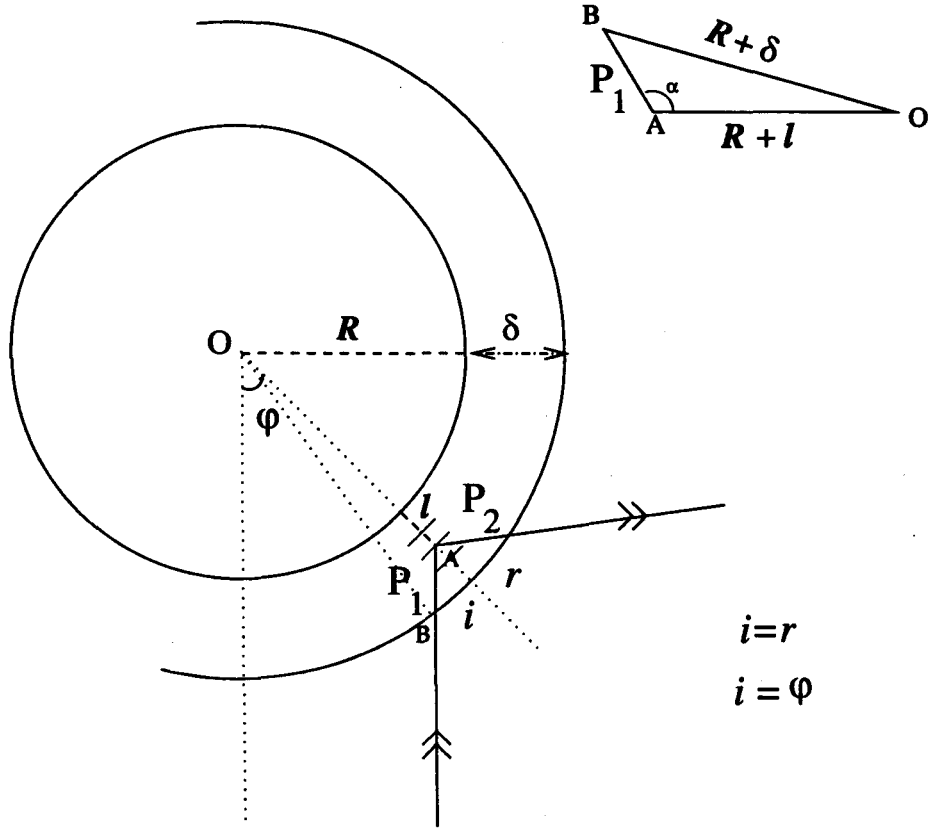


**Figure 2.7: Calculation of the path traveled by x-rays inside the sample.** The inner circle of radius  $R$  is the beaker, the sample is of thickness  $\delta$ .  $P_1$  and  $P_2$  are the paths traveled by the x-rays (marked by double arrow) before and after reflection from the sample. To calculate  $P_1$ , the triangle  $OAB$  is considered. From geometrical considerations, the Bragg angle  $\theta = \pi/2 - \phi$ . Also, angle  $\alpha = \pi - \phi$ . Therefore, applying the rules of trigonometry to triangle  $OAB$ ,  $P_1$  is given by  $-(R + l)\sin(\theta) + [(R + \delta)^2 - (R + l)\cos^2(\theta)]^{\frac{1}{2}}$ . Since the rays are Bragg reflected, from the laws of reflection and geometry it can be shown that,  $P_2 = P_1$ . Therefore,  $p(l) = 2P_1(l)$ .

fitting procedure first used by Sun et. al. [7] in the context of the  $P_{\beta'}$  phase. In this approach, a function representing the electron density in one unit cell of the  $P_{\beta'}$  phase (in real space) is first constructed such that this function incorporates known and plausible features of the structure. This function has free parameters built into it to account for the imprecisely known features. This trial function is Fourier transformed to get the trial diffraction pattern (eq.-2.1). The values of these parameters are determined by a standard least squares fitting procedure where the calculated structure factors are fitted to the observed structure factors. The Fourier components corresponding to the final fitted parameters yield the phases of the reflections. These phases are now combined with the observed intensities and inverse Fourier transformed to give the final electron density map (eq.-2.1). The electron density  $\rho(x, z)$  at a point  $(x, z)$  is given by:

$$\rho(x, z) = \sum_h \sum_k \Phi_c^{hk} |F_o^{hk}| \cos(q_x^{hk} x + q_z^{hk} z)$$

where  $\Phi_c^{hk}$  is the phase calculated from the fit and  $|F_o^{hk}|$  the observed structure factor for a spot with Miller indices  $(h, k)$ . A schematic diagram representing the above procedure is given in figure-2.8. The modeling step is crucial since a wrong or bad model may not lead to the correct structure. It is important to look at the final electron density map and accept it only if there are no features that are known to be obviously incorrect.

The electron density within the unit cell,  $\rho(x, z)$ , is described as the convolution of a ripple contour function  $C(x, z)$  and the transbilayer electron density profile  $T_\psi(x, z)$ :

$$\rho(x, z) = C(x, z) * T_\psi(x, z)$$

The ripple contour function is written as  $C(x, z) = \delta(z - u(x))$ , where  $u(x)$  describes the ripple profile. In reciprocal space the convolution becomes a simple multiplication. The structure factor  $F(\mathbf{q})$  is therefore given by

$$F(\mathbf{q}) = F_C(\mathbf{q})F_T(\mathbf{q})$$

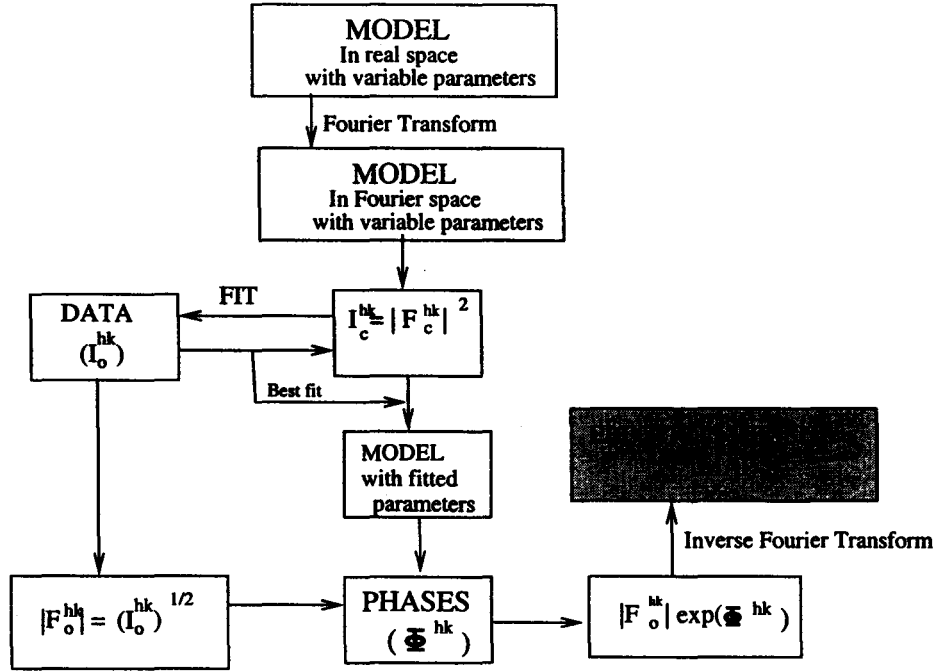


Figure 2.8: A schematic diagram of the fitting procedure.

where  $F_C(\mathbf{q})$  and  $F_T(\mathbf{q})$  are the Fourier transforms of  $C(x, z)$  and  $T_\psi(x, z)$  respectively.

#### 2.4.1 Specific forms of $C(x, z)$ and $T_\psi(x, z)$

**Ripple shape:  $C(x, z)$**

The ripple shape is taken to have the form of a saw-tooth with peak-to-peak amplitude  $A_r$ .  $\lambda_1$  is the projection of the longer arm of the saw-tooth on the x-axis (figure-2.9).

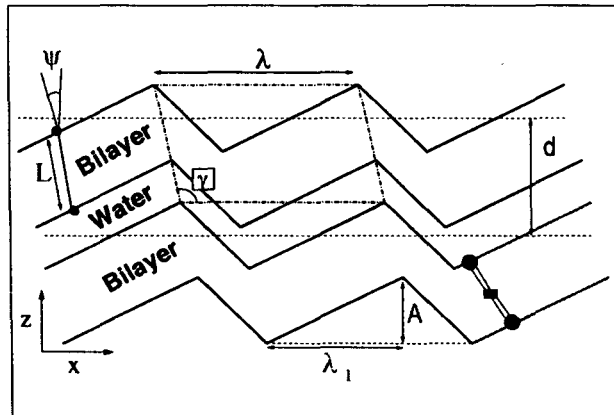


Figure 2.9: Schematic showing the structural parameters of the ripple phase.



This is exactly same as the shape considered in ref. [7]. The origin of the unit cell is chosen such that the ripple profile is explicitly centrosymmetric. Then the shape function  $u(x)$  is given by:

$$u(x) = \begin{cases} -\frac{A_r}{\lambda_r - \lambda_1} \left(x + \frac{\lambda_r}{2}\right) & \text{if } -\frac{\lambda_r}{2} \leq x < -\frac{\lambda_1}{2} \\ \frac{A_r}{\lambda_1} x & \text{if } -\frac{\lambda_1}{2} \leq x \leq \frac{\lambda_1}{2} \\ -\frac{A_r}{\lambda_r - \lambda_1} \left(x - \frac{\lambda_r}{2}\right) & \text{if } \frac{\lambda_1}{2} < x \leq \frac{\lambda_r}{2} \end{cases}$$

Therefore,

$$F_C(\mathbf{q}) = \frac{1}{\lambda_r} \int_{-\frac{\lambda_r}{2}}^{\frac{\lambda_r}{2}} dx \, dz \, e^{i[q_x x + q_z z]} \delta(z - u(x)) \quad (2.7)$$

$$= \frac{1}{\lambda_r} \int_{-\frac{\lambda_r}{2}}^{\frac{\lambda_r}{2}} dx \, e^{i[q_x x + q_z u(x)]} \quad (2.8)$$

$$= \frac{\lambda_1}{\lambda_r} \text{sinc}(\omega) + \frac{\lambda_r - \lambda_1}{\lambda_r} \frac{\cos \frac{1}{2} \left( \frac{1}{2} q_x \lambda_r + \omega \right)}{\cos \frac{1}{2} \left( \frac{1}{2} q_x \lambda_r - \omega \right)} \\ \times \text{sinc} \left( \frac{q_x \lambda_r}{2} - \omega \right)$$

where  $\text{sinc}(\omega) \equiv \frac{\sin(\omega)}{\omega}$  and

$$\omega = \frac{1}{2} (q_x \lambda_1 + q_z A_r)$$

$q_x$  and  $q_z$  are given in eq.-2.3 in terms of the Miller indices and the lattice parameters.

$\lambda_1$  and  $A_r$  are the adjustable parameters.

### A different $C(x, z)$

A different, more smooth initial model was also tried for  $C(x, z)$  to check if the final shape is an artifact of the specific initial model. Here

$$u(x) = a \sin\left(\frac{2\pi x}{\lambda_r}\right) + b \sin\left(\frac{4\pi x}{\lambda_r}\right) \quad (2.9)$$

$a$  and  $b$  are the adjustable parameters.

### Trans-bilayer profile ( $T_\psi(x, z)$ )

$T_\psi(x, z)$  gives the electron density at any point  $(x, z)$  in the bilayer along a straight line, which makes an angle  $\psi$  with the  $z$ -axis. The electron density in the methylene region of the bilayer is close to that of water and is taken as zero. We have used

three models for  $T_\psi(x,z)$ , two of which are equivalent to the SDF and M1G models of ref. [7]. (model I and II below respectively).

**Model I:** In model I,  $T_\psi(x,z)$  is taken as consisting of two delta functions with positive coefficients  $\rho_H$ , corresponding to the head group regions separated by a distance  $L$ , and a central delta function with negative coefficient of magnitude  $\rho_M$ , corresponding to the methyl region. The variable head-to-head distance  $L$  accounts for both chain melting and a tilt in the direction perpendicular to the rippling direction. This can be represented by

$$T_\psi(x, z) = \delta(x + z \tan\psi) \{ \rho_H [\delta(z - \frac{L}{2} \cos\psi) + \delta(z + \frac{L}{2} \cos\psi)] - \rho_M \delta(z) \} \quad (2.10)$$

Taking Fourier transform,

$$F_T(\mathbf{q}) = \rho_m \{ (\rho_H/\rho_M) \cos(q_z \frac{L}{2} \cos\psi - q_x \frac{L}{2} \sin\psi) - 1 \} \quad (2.11)$$

The adjustable parameters here are:  $\psi$ ,  $\frac{\rho_H}{\rho_M}$  and  $L$  (see figure-2.9).

**Model II:** The head groups and the chains can be more realistically modeled by replacing the delta functions representing the head groups and chains by Gaussians of width  $\sigma_h$  and  $\sigma_m$ , respectively. The electron density in the minor arm is allowed to be different by a factor  $f_1$  from that in the major arm. The region where the two arms meet is modeled as a wall with an electron density differing by a factor  $f_2$  from the rest of the arm. The wall thickness in this model is fixed at a value that is small compared to the bilayers thickness, half of the wall region being in each arm. The final form factor  $F(\mathbf{q})$  reads:

$$F(\mathbf{q}) = F_C^M \cdot F_T^M + f_1 F_C^m \cdot F_T^m + f_2 (F_C^{M'} \cdot F_T^M + f_1 F_C^{m'} \cdot F_T^m) \quad (2.12)$$

where  $F_C^M$  and  $F_C^m$  are the contributions to  $F_C$  from the major and minor arms respectively and  $F_T^M$  and  $F_T^m$  are the respective contributions to  $F_T$ . The prime indicates that the contribution comes from the wall region. The Fourier transform of the transbilayer profile for the major arm is:

$$F_T^M = \frac{\rho_{H1}}{\rho_{M1}} e^{-\sigma_{h1}^2 \frac{(q_z - q_x \tan\psi_1)^2}{2}} \cos(q_z \frac{L_1}{2} \cos\psi_1 - q_x \frac{L_1}{2} \sin\psi_1) - e^{-\sigma_{m1}^2 \frac{(q_z - q_x \tan\psi_1)^2}{2}} \quad (2.13)$$

and for the minor arm is:

$$F_T^m = \frac{\rho_{H_2}}{\rho_{M_2}} e^{-\sigma_{h_2}^2 \frac{(q_z - q_x \tan \psi_2)^2}{2}} \cos\left(q_z \frac{L_2}{2} \cos \psi_2 - q_x \frac{L_2}{2} \sin \psi_2\right) - e^{-\sigma_{m_2}^2 \frac{(q_z - q_x \tan \psi_2)^2}{2}} \quad (2.14)$$

The labels 1 and 2 refer to the major and minor arm, respectively. In this model the following conditions are imposed:

$$L_1 = L_2, \sigma_{h_1} = \sigma_{h_2}, \sigma_{m_1} = \sigma_{m_2}, \frac{\rho_{H_1}}{\rho_{M_1}} = \frac{\rho_{H_2}}{\rho_{M_2}} \text{ and } \psi_1 = \psi_2 \quad (2.15)$$

The shape function  $u(x)$  is the same as eq.-2.7 but now the calculation of the Fourier transforms for the minor and major arm and also the wall region (eq.-2.8) has to be done separately. There are 10 adjustable parameters in this model.

**Model III:** In the models I and II, the head-to-head distance  $L$  is fixed along a direction making an angle  $\psi$  w.r.t the  $z$ -axis. This forces bilayer thicknesses along the layer normal to be different in the two arms. Therefore in model III, the restrictions imposed upon the models I and II were lifted, so that the length  $L$  of the chains in the two arms need not be the same. The parameters  $L$ ,  $\psi$ ,  $\sigma_h, \sigma_m$  and  $\rho_H/\rho_M$  were allowed to be different in the two arms of the ripple.

$$L_1 \neq L_2, \sigma_{h_1} \neq \sigma_{h_2}, \sigma_{m_1} \neq \sigma_{m_2}, \frac{\rho_{H_1}}{\rho_{M_1}} \neq \frac{\rho_{H_2}}{\rho_{M_2}} \text{ and } \psi_1 \neq \psi_2 \quad (2.16)$$

The expressions for  $F_T^M$  and  $F_T^m$  are same as in equations-2.13 and -2.14 except that now the equalities-2.15 are not imposed. Further, the wall between the two arms was taken to have a variable width  $w$ . This model has 15 adjustable parameters. Minimization is done by iterative least squares fitting with respect to six variables at a time [8].

## 2.5 The fitting procedure

The adjustable parameters (henceforth referred to as  $a_i$  s) in the models discussed above are determined by a non-linear least squares fitting procedure that uses the Lavenberg-Marquardt Method [8]. In this method some initial value is chosen for each  $a_i$ . The  $F(\mathbf{q})$  corresponding to each observed reflection is calculated. Let the

estimated  $F(\mathbf{q})$  for a spot with Miller indices  $(h, k)$  be  $F_e^{hk}$ . Let the square-roots of the observed intensities with the same Miller indices be  $|F_o^{hk}|$ . Then the deviation is given by:

$$\Sigma = \sum_{h,k} || F_e^{hk} | - | F_o^{hk} ||^2$$

This quantity is minimized using the conjugate gradient method [8]. In this method, not only the function to be minimized ( $\Sigma$ ) but also the derivatives of this function with respect to all the parameters ( $\frac{\partial \Sigma}{\partial a_i}$ ) have to be supplied. The derivatives were determined analytically with the help of the mathematical software package 'Maple'. The final converged values of the  $a_i$  s are put back into the expression for  $F_e^{hk}$  to get the best-fit structure factors  $F_f^{hk}$ . The phase  $\Phi_c^{hk}$  of the spot with Miller indices  $(h, k)$  is  $\frac{F_f^{hk}}{|F_f^{hk}|} = \pm 1$  (since the structure is centro-symmetric). The product of  $F_o^{hk}$  and  $\Phi_c^{hk}$  is calculated to give the final set of  $F(\mathbf{q})$  s which is then inverse Fourier transformed to get the electron density maps.

## 2.6 Conclusion

In this chapter we have discussed the details of our experimental and data reduction procedure. We have shown that absorption corrections do not significantly change the calculated electron density profiles. We are unable to analyze the data from oriented samples using models II and III, due to the lack of convergence resulting from the large number of adjustable parameters in these models. The shape function given by eq.-2.9 also leads to a similar lack of convergence in case of oriented samples. Hence all the data from oriented samples were analyzed only with  $T_\psi(x, z)$  given by model I and  $C(x, z)$  given by a sawtooth shape.. The electron density maps obtained using the procedure described in this chapter will be discussed in chapter-III.

# Bibliography

- [1] D. Sherwood, Crystals, X-rays and Proteins, Longman, 1976.
- [2] D. C. Wack and W. W. Webb, Phys. Rev. A **40**, 2712 (1989).
- [3] J. Katsaras and V. A. Raghunathan, Phys. Rev. Lett. **74**, 2022 (1995).
- [4] A. Tardieu, V. Luzzati, and F. C. Reman, J. Mol. Biol. **75**, 711 (1973).
- [5] M. J. Janiak, D. M. Small, and G. G. Shipley, J. Biol. Chem. **254**, 6068 (1979).
- [6] M. C. Wiener, R. M. Suter and J. F. Nagle, Biophys. J., **55**, 315 (1989).
- [7] W.-J. Sun, S. Tristram-Nagle, R. M. Suter, and J. F. Nagle, Proc. Natl. Acad. Sci. USA **93**, 7008 (1996).
- [8] W.H. Press, S.A. Teukolsky, W.T.Vellerling, and B.P. Flannery, Numerical Recipes in C, Cambridge University Press, 1997.